Biophysical Journal, Volume *115*

Supplemental Information

Microtubule Dynamics, Kinesin-1 Sliding, and Dynein Action Drive Growth of Cell Processes

Dietmar B. Oelz, Urko del Castillo, Vladimir I. Gelfand, and Alex Mogilner

Supplementary Material for Microtubule dynamics, kinesin-1 sliding and dynein action drive growth of cell processes

D. B. Oelz, U. del Castillo, V. I. Gelfand, A. Mogilner

August 9, 2018

1 Additional supplementary figures

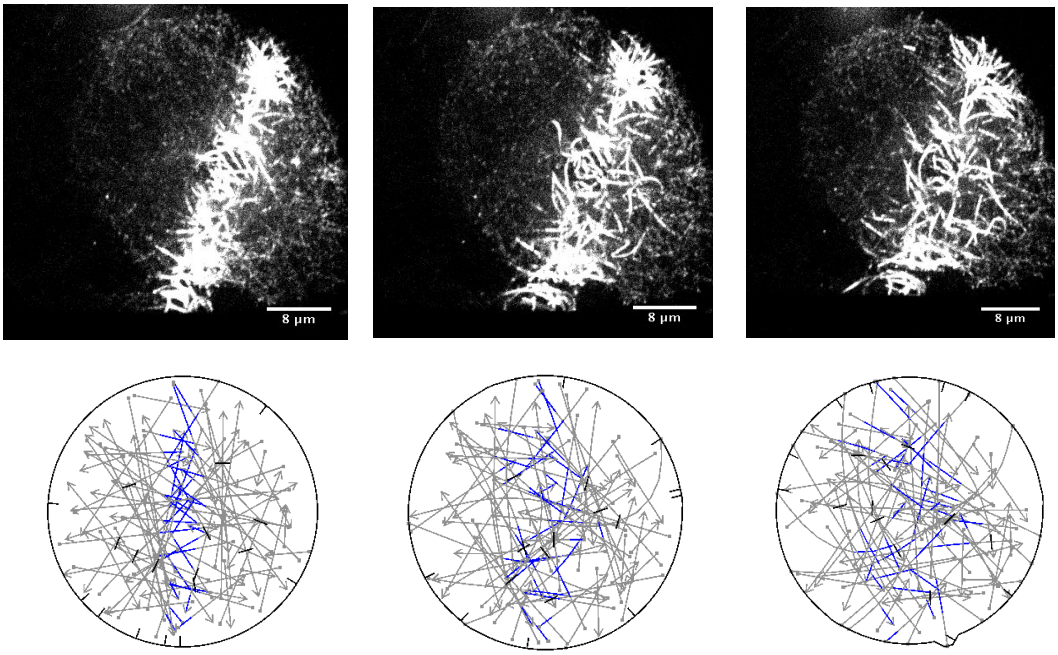

Figure S 1: Upper row: MTs in S2 cells expressing photoconvertible EOS2-tubulin were stabilized with 40nM taxol. MTs in a stripe in the center of the cell were photoconverted from green to red and fluorescence in the red channel was recorded. Three consecutive images in the top row are taken 1 min apart. Lower row: Snapshots from one simulation of the MT network with 10 active kinesin motors and $N = 75$ MTs at 1 minute intervals. Both dynein and kinesin motors are shown in black. Fluorescent MT segments after photoconversion are shown in blue.

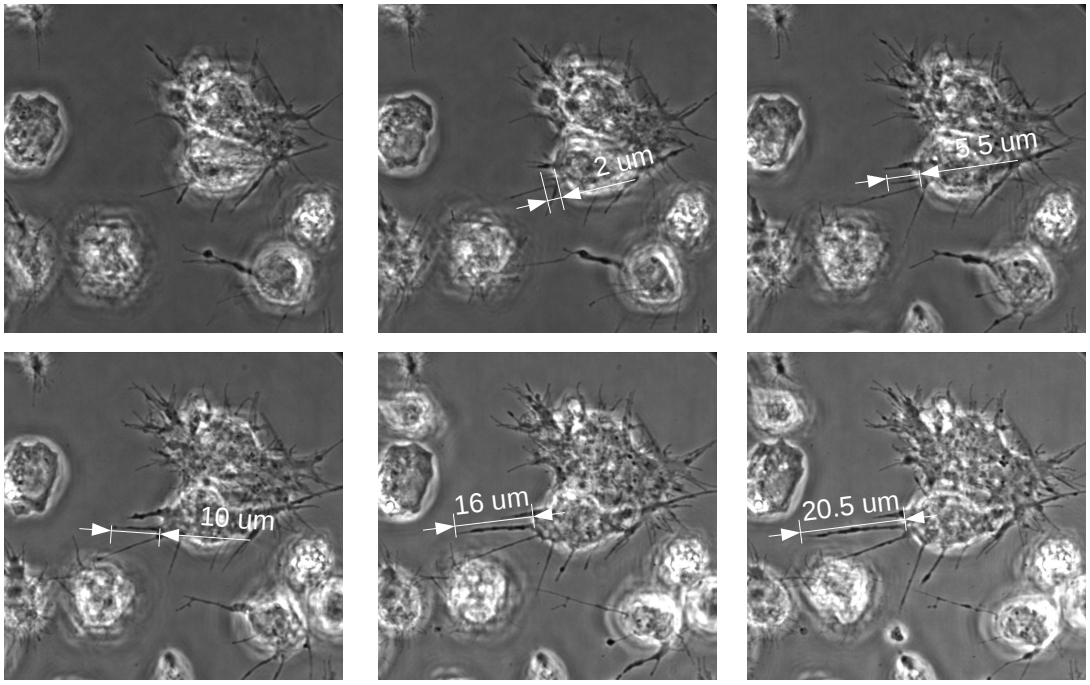

Figure S 2: Measurement of process growth in control cells. Images taken at $t = 28, 32, 40, 48, 60, 72$ min.

2 Details of the computational model

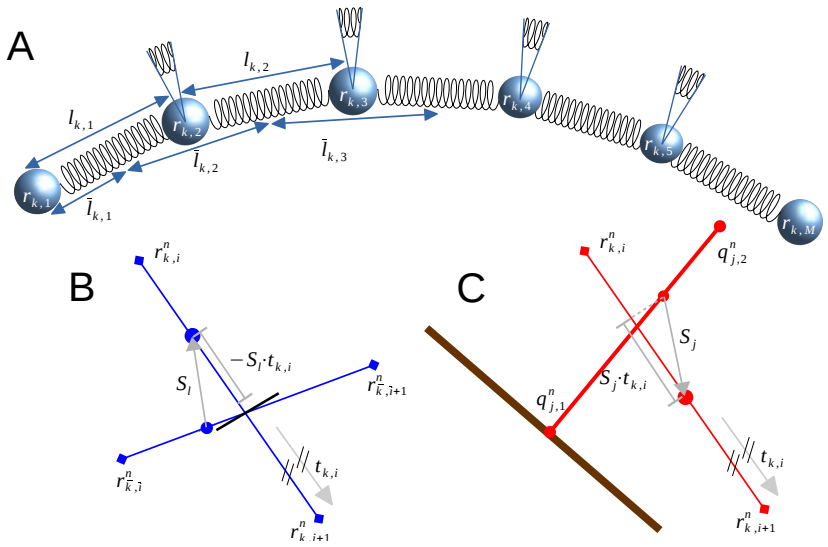

Figure S 3: Details of the computational model. A: Representation of MTs as chains of nodes and springs. B: Model representation of kinesin motors at the intersection of two segments of intersecting MTs. C: Representation of dynein motors as stiff bars crossing the segment of a MT.

2.1 Computational Model

There is a fixed number of M MTs. Each MT with index k is represented by a chain of N_k^n nodes positioned at $r_{k,i}^n$ ($i = 1, ..., N_k^n$, and $r_{k,i}^n$ is a vector in 2D) at the n^{th} moment in time ($n = 1, 2, \ldots$ is the index of the computational step). The model mechanics can be gleaned from Fig. S3 and Fig. S4.

The central part of our mathematical model is the following system of force balance equations which we solve at every time step to update the positions of the MT nodes:

$$\mathbf{F}_{k,i}^{\text{drag}} + \mathbf{F}_{k,i}^{\text{comptens}} + \mathbf{F}_{k,i}^{\text{bend}} + \mathbf{F}_{k,i}^{\text{therm}} + \mathbf{F}_{k,i}^{\text{boundary}} + \sum_{j=1}^{N^{\text{dynein}}} \mathbf{F}_{j,k,i}^{\text{dynein}} + \sum_{l=1}^{N^{\text{kinesin}}} \mathbf{F}_{l,k,i}^{\text{kinesin}} = 0 \,. \qquad (1)$$

In what follows we detail the terms of this system of equations.

1. The equilibrium length of the segment between the nodes i and $i+1$ is $l_{k,i}^n$; the segment is a stiff linear spring deformations of which generate the force of tension/compression:

$$\mathbf{F}_{k,i}^{\text{comptens}} = -\frac{\kappa_S}{2} \frac{\delta}{\delta \mathbf{r}_{k,i}^n} \sum_{i=1}^{N_k^n} (|\mathbf{r}_{k,i+1}^n - \mathbf{r}_{k,i}^n| - l_{k,i}^n)^2 \,.$$

   The large value we use for κ_S (Table S 1) guarantees that the simulated MTs have appropriately high longitudinal stiffness.

2. Movement of a node is associated with the viscous drag force, which is proportional to the lengths of the two segments adjacent to the node and to the velocity of the node:

$$\mathbf{F}_{k,i}^{\text{drag}} = \gamma \, \bar{l}_{k,i}^n \frac{\mathbf{r}_{k,i}^n - \mathbf{r}_{k,i}^{n-1}}{\Delta t} \quad \text{where} \quad \bar{l}_{k,i}^n = \begin{cases} l_{k,i}^n/2 & i = 1 \,,\ N_k^n \,, \\ (l_{k,i}^n + l_{k,i-1}^n)/2 & 1 < i < N_k^n \,. \end{cases}$$

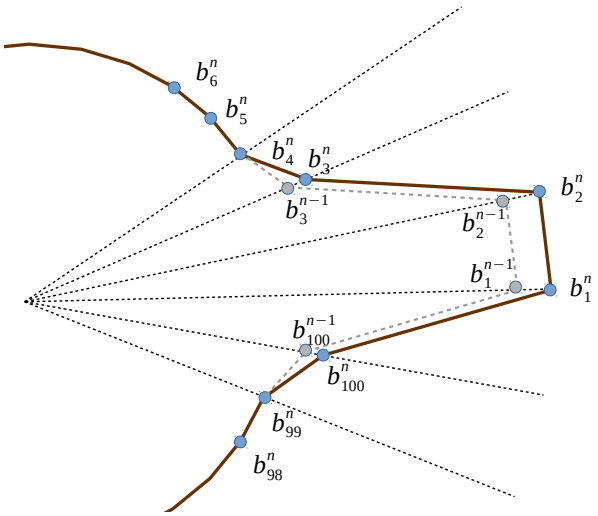

Figure S 4: Computational implementation of the process growth. Short processes are elongated by simultaneously shifting the two nodes at the tip of the process in the radial direction. Their two neighboring nodes are also shifted radially by a proportional distance. Long processes are elongated only at the tips, in a way such that the distance between the nodes at the tip does not change.

3. The thermal force on a node is given by the standard formula:

$$\mathbf{F}_{k,i}^{\text{therm}} = \sqrt{\frac{2\,k_B T\,\gamma\,\bar{l}_{k,i}^n}{\Delta t}}\;\theta_{k,i}^n\;,$$

where the random number $\theta_{k,i}^n$ is drawn from the standard normal distribution and the magnitude of the force is proportional to the square root from the thermal energy divided by the effective diffusion coefficient (calculated from Einstein's formula) (11). Note that proportionality of the force to the factor $1/\sqrt{\Delta t}$, where Δt is the computational time step interval, ensures that the consecutive Brownian movement's displacements are as prescribed by thermodynamics.

4. Elastic bending forces are given by:

$$\mathbf{F}_{k,i}^{\text{bend}} = -\frac{\kappa}{2}\frac{\delta}{\delta \mathbf{r}_{k,i}^n}\sum_{i=2}^{N_k^n-1}\frac{(\mathbf{t}_{k,i}^n - \mathbf{t}_{k,i-1}^n)^2}{\bar{l}_{k,i}^n}\;,$$

where the normalized segment direction is given by $\mathbf{t}_{k,i}^n = (\mathbf{r}_{k,i+1}^n - \mathbf{r}_{k,i}^n)/l_{k,i}^n$.

5. Forces due to steric repulsion from the boundary are given by:

$$\mathbf{F}_{k,i}^{\text{boundary}} = -10^7 \times \frac{\partial}{\partial \mathbf{r}_{k,i}^n}\frac{d(\mathbf{r}_{k,i}^n)^3}{3}\;,$$

where $d = d(\mathbf{x})$ is zero for any point within the polygon that represents the cell area (Fig. S4) and otherwise it is defined as the shortest distance to the boundary.

6. Dynein motors at the boundary are represented by stiff bars with endpoints at $q_{j,1}^n$ and $q_{j,2}^n$ such that $q_{j,2}^n - q_{j,1}^n$ is orthogonal to the boundary segment along which the point $q_{j,1}^n$ is located (Fig. S3 C). The point $\mathbf{x}$ at which the dynein segment intersects a MT segment is expressed as and can be found as the solution of:

$$\mathbf{x} = \alpha\,\mathbf{r}_{k,i+1}^{n-1} + (1-\alpha)\,\mathbf{r}_{k,i}^{n-1} = \beta\,\mathbf{q}_{j,2}^{n-1} + (1-\beta)\,\mathbf{q}_{j,1}^{n-1}\;.$$

Table S 1: List of parameters.

Description	Symbol	Value	Reference
Spring constant (microtubule node separation)	κ_S	$100\,\mathrm{pN\,\mu m^{-1}}$	almost inextensible & incompressible
Drag on microtubules	γ	$1.4\,\mathrm{pN\,\mu m^{-2}\,sec}$	$\frac{3\pi\eta}{\log(10\,\mu\mathrm{m}/r)}$ (1)
Radius of microtubules	r	$0.0125\,\mu\mathrm{m}$	(2)
Viscosity of cytoplasm	η	$1\,\mathrm{pN\,sec\,\mu m^{-2}}$	1000× water (3)
Bending elasticity	κ	$10\,\mathrm{pN\,\mu m^2}$	(4)
Length of MT segment in simulations	l_s	$0.2\,\mu\mathrm{m}$	chosen to be much smaller than characteristic MT length
Off-rate of kinesin motors	ζ_{kin}	$0.1\,\mathrm{sec^{-1}}$	(5)
Off-rate of dynein motors	ζ_{dyn}	$0.1\,\mathrm{sec^{-1}}$	(5)
Turnover (random repositioning along the cortex) rate of dynein motors	κ_{dyn}	$0.05\,\mathrm{sec^{-1}}$	estimated
Number of microtubules	N	150	chosen for numerical convenience
Number of simultaneously bound kinesin motors	M_k	20	fitting experimental results (Fig. 1)
Density of dynein motors	M_d	$0.25/\mu$ m	fitting experimental results
Effective spatial range of a dynein motor	l_d	$0.75/\mu\mathrm{m}$	based on thickness of actin cortex (6)
Cell radius	R_0	$10\,\mu\mathrm{m}$	(7)
Number of straight cortex segments	K_c	100	chosen for numerical convenience
Threshold value for process initiation and elongation	F_p	3 pN	estimated to reproduce experimental results (Fig. 1 C)
Rate of process elongation	V_p	$0.1\,\mu\mathrm{m\,sec^{-1}}$	estimated to reproduce experimental results (Fig. 1 C)
Stall force of dynein motors	F_s^{dynein}	1.36 pN	(8)
Force free velocity of dynein motors	V_m^{dynein}	$0.86\,\mu\mathrm{m\,sec^{-1}}$	(8)
Stall force of kinesin motors	F_s^{kinesin}	4.7 pN	(8)
Force free velocity of kinesin motors	V_m^{kinesin}	$0.57\,\mu\mathrm{m\,sec^{-1}}$	(8)
Thermal energy	k_BT	$0.004\,\mathrm{pN\,\mu m}$	(9)

Namely, $\mathbf{x}$ is a convex combination ($0 \leq \alpha \leq 1$) of either the endpoints of the MT segment, or ($0 \leq \beta \leq 1$) of the endpoints of the dynein segment. The vector of the displacement of the intersection between the MT and dynein segments within one time step,

$$\mathbf{S}_j = \alpha\,\mathbf{r}^n_{k,i+1} + (1-\alpha)\,\mathbf{r}^n_{k,i} - (\beta\,\mathbf{q}^n_{j,2} + (1-\beta)\,\mathbf{q}^n_{j,1})\ ,$$

is projected onto the directional vector of the MT segment $\mathbf{t}^n_{k,i}$ in order to setup a varia-

Table S 2: List of parameters for microtubule dynamic instability.

Description	Symbol	Value	Reference
Reference force to halt microtubule growth	F_{halt}	0.5 pN	estimated
MT dynamics: rate of transition from growth to pause	κ_1	$0.07\,\text{sec}^{-1}$	(10)
MT dynamics: rate of transition from pause to catastrophy	κ_2	$0.5\,\text{sec}^{-1}$	estimated
MT dynamics: rate of transition from shortening to pause	κ_3	$0.14\,\text{sec}^{-1}$	(10)
MT dynamics: rate of transition from pause to growth	κ_4	$0.5\,\text{sec}^{-1}$	estimated
Microtuble growth rate	v_g	$0.15\,\mu\text{m}\,\text{sec}^{-1}$	(10)
Microtubule shortening rate	v_s	$0.3\mu\text{m sec}^{-1}$	(10)

tional formulation of a linear force-velocity relation for dynein motors:

$$\mathbf{F}^{\text{dynein}}_{j,k,i} = -\frac{\delta}{\delta \mathbf{r}^n_{k,i}} F^{\text{dynein}}_s \left(-\mathbf{S}_j \cdot \mathbf{t}^n_{k,i} + \frac{|\mathbf{S}_j|^2}{2\,\Delta t\, V^{\text{dynein}}_m} \right) ,$$

in which the second term in the bracket accounts for the linear attenuation of the motor force by the motor velocity. The resulting force is in the direction of the MT minus-end.

7. Analogously, the kinesin-1 force, applied to the intersection of two MT segments at

$$\mathbf{x} = \alpha\, \mathbf{r}^{n-1}_{k,i+1} + (1-\alpha)\, \mathbf{r}^{n-1}_{k,i} = \beta\, \mathbf{r}^{n-1}_{\bar{k},\bar{i}+1} + (1-\beta)\, \mathbf{r}^{n-1}_{\bar{k},\bar{i}} ,$$

where the motor domain attaches to the MT with index k and the cargo domain - to the MT with index $\bar{k}$ (Fig. 3B), depends on the displacement of this intersection, $\mathbf{S}_l$, within one time step:

$$\mathbf{S}_l = (\alpha\, \mathbf{r}^n_{k,i+1} + (1-\alpha)\, \mathbf{r}^n_{k,i}) - (\beta\, \mathbf{r}^n_{\bar{k},\bar{i}+1} + (1-\beta)\, \mathbf{r}^n_{\bar{k},\bar{i}}) .$$

The variational formulation of the force exerted by the kinesin-1 motor protein in the direction of the plus end of the MT k with index k is given by:

$$\mathbf{F}^{\text{kinesin}}_{l,k,i} = -\frac{\delta}{\delta \mathbf{r}^n_{k,i}} F^{\text{kinesin}}_s \left(\mathbf{S}_l \cdot \mathbf{t}^n_{k,i} + \frac{|\mathbf{S}_l|^2}{2\,\Delta t\, V^{\text{kinesin}}_m} \right) .$$

The opposing force is applied to the MT with index $\bar{k}$.

At every time step our simulations consist of three sub-steps:

1. Simulate the turnover (dissociation and re-association at new locations) of molecular motors.

2. Solve the system of force balance equations Eq. 1 to obtain the new positions and configurations of the MTs. Note that numerically we solve the energy minimization problem the solution of which satisfies Eq. 1. The components of the energy functional are chosen such that their variations correspond to the forces listed in Eq. 1. We emphasize though that the system is away from thermal equilibrium, and the energy functional does not correspond to actual physical free energy. This is just a mathematical technique convenient for the computation; the resulting forces have the standard form that was used many times before in modeling studies.

3. Evaluate $\mathbf{F}_{k,i}^{\text{boundary}}$ locally for every tip of a process and every segment of the boundary that is not part of a process. If the threshold force value is exceeded, initiate, respectively elongate the process by the distance $\Delta t\, V_p$.

4. MT dynamics: Every MT cycles through the following four states: growing, pause 1, shortening, pause 2 and proceeds to the next state at random times, according to the respective transition rates listed in Table 1. In addition, MTs which shrink to a minimum length of 0.2 µm immediately proceed to state pause 2 ("rescue"). On the other hand, MTs which experience mechanical load at the plus ends are also more likely to proceed to the next state: The force $F = \mathbf{F}_{k,i}^{\text{boundary}} \cdot (-t_{k,N_k^n-1})$, i.e. component of the force from the membrane parallel to the MT tip, corresponds to the pressure onto the plus end of MT with index k and upregulates the transition rate to pause 1 according to the Bell law: $\kappa_1 \exp(F/F_{\text{halt}})$.

3 Additional notes on the model and comparison of the numerical and experimental results.

As is shown in Fig. 4, the simulations predict roughly the same average process lengths as the experimental data. However, the variance in lengths is much greater in the experiment, and also the longest observed processes are much longer than the longest processes predicted by the model. It is likely that the greater variance in the experiments is associated with complex factors that the model does not take into account. Three of these factors are 1) dynamic adhesions of the process to the substrate; 2) MT associated proteins other than motors; 3) 3D geometry of the processes, rather than the idealized 2D model geometry. Also, the longest observed processes could be associated with augmin-mediated MT nucleation or branching from other MTs in the processes, as well as by changes in MT dynamics in the processes due to interactions with the adhesions.

We assumed in the model that the force generated by kinesin on the intersection between two MTs is directed parallel to the MT with the motor domain on it and has magnitude that is independent on the intersection angle. In principle, either the motor force magnitude or the force direction, or both, could be functions of the MT intersection angle. If the force generated by the motor domain decreases when the angle between the intersecting MTs increases, it is easy to imagine (and we confirmed this with a few trial simulations) that the MTs would be moving less frequently and more slowly, and as a result, the processes would grow slower. However, this trend can be offset by an increase of the working kinesin numbers. We have not attempted systematic simulations of this more complex model because we have no data on the angular force dependence, and also ignoring this possible effect is not the main simplification of the model.

In the simulations the cortex was split into 100 segments for the following reasons. When testing the model, this number was varied, and we found that when the number of segments was significantly smaller, then the number of the generated processes was, predictably, smaller (and the zigzag boundary looked less realistic). The rates of the processes' growth were slightly different, because of the variety of mutually opposing factors: on the one hand, on the average, a greater number of MTs entered artificially wider processes; on the other hand, dyneins could not reach some of the MTs. When the segment number was increased above 100, neither the number of generated processes, nor the rate of the process growth, depended sensitively on the segment number. The reasons are: According to the model, it is the number of MTs that are propelled (by kinesins) more or less perpendicularly to the cell boundary outward that limits the number of the cell processes initiated. As far as this number is significantly smaller, than the number of boundary segments, finer segmentation does not affect the process number. After the processes start to grow, they become traps for other MTs growing or being propelled outward, and new processes rarely appear long after 10 processes grow significantly. The initial force

to induce the process is independent of the segment size in the model, and so a single MT propelled by a single kinesin perpendicularly to the boundary rarely fails to initiate the process. As was discussed in the manuscript, the rate of the process growth is limited mostly by the MT dynamics and kinetics of the motor action, and so is not very sensitive to the net motor force. For all these reasons, we chose to divide the boundary into 100 segments in the simulations.

4 Experimental methods

Drosophila **S2 cultures:** S2 cells were cultured in Insect-Xpress media (Lonza) at 25°C. For MT sliding experiments in S2 cell, a stable cell line expressing pMT-tdEOS-tubulin was created using Effecten transfection kit (Qiagen). Expression of pMT construct was induced by adding 200 μM CuSO4 to the media for 48 h. To induce the formation of microtubule-based processes, S2 cells were plated in media supplemented with 2.5 μM Cytochalastin D. To block microtubule dynamics, addition of 40 nM Taxol was added right before imaging. To knockdown Dynein levels, S2 cell cultures at 1.5×10^6 cells/mL were treated twice (on day 1 and 3) with 20 μg of double-stranded RNA targeting Dynein Heavy Chain sequence. Cell analysis was performed on day 5.

Microscopy and imaging: All microscopy images were acquired using a Nikon (Tokyo, Japan) Eclipse U2000 inverted microscope at 25 °C. To image microtubule sliding in S2 cells, a Yokogawa CSU10 spinning disk confocal head, Nikon Perfect Focus system, and 100x/1.45- N.A. objective was used. Images were acquired with an Evolve EMCCD (Photometrics) controlled Nikon NIS-Elements software (AR 4.00.07). S2 cells expressing tdEOS-tubulin were photoconverted for 5 sec using 405 nm light from a light emitting diode light source (89 North Heliophor), which was constrained to a rectangular slit. To image process formation in S2 cells, a Nikon Perfect Focus system, a 100x1.4- Ph3 Plan APO objective and a digital CMOS, ORCA-Flash4.0 V2 C11440-22CU (Hamamatsu Photonics, Hamamatsu, Japan) controlled by MetaMorph, version 7.7.7.0 (Molecular Devices, Sunnyvale, CA) was used. Phase-contrast images were illuminated using a CoolLED PrecisExcite (Hampshire, UK).

References

1. Berg, H., 1993. Random Walks in Biology. Princeton paperbacks. Princeton University Press.

2. Alberts, B., A. Johnson, J. Lewis, D. Morgan, M. Raff, K. Roberts, and P. Walter, 2014. Molecular Biology of the Cell. 500 Tips. Garland Science.

3. Luby-Phelps, K., 2000. Cytoarchitecture and physical properties of cytoplasm: volume, viscosity, diffusion, intracellular surface area. *Int. Rev. Cytol.* 192:189–221.

4. Kikumoto, M., M. Kurachi, V. Tosa, and H. Tashiro, 2006. Flexural Rigidity of Individual Microtubules Measured by a Buckling Force with Optical Traps. *Biophysical Journal* 90:1687 – 1696.

5. Schroeder, H., A. G. Hendricks, K. Ikeda, H. Shuman, V. Rodionov, M. Ikebe, Y. Goldman, and E. Holzbaur, 2012. Force-Dependent Detachment of Kinesin-2 Biases Track Switching at Cytoskeletal Filament Intersections. *Biophysical Journal* 103:48 – 58.

6. Clark, A. G., K. Dierkes, and E. K. Paluch, 2013. Monitoring actin cortex thickness in live cells. *Biophys. J.* 105:570–580.

7. Rogers, S., and G. Rogers, 2008. Culture of Drosophila S2 cells and their use for RNAi-mediated loss-of-function studies and immunofluorescence microscopy. *Nature Protocols* 3:606–611.

8. Kunwar, A., S. K. Tripathy, J. Xu, M. K. Mattson, P. Anand, R. Sigua, M. Vershinin, R. J. McKenney, C. C. Yu, A. Mogilner, and S. P. Gross, 2011. Mechanical stochastic tug-of-war models cannot explain bidirectional lipid-droplet transport. *Proceedings of the National Academy of Sciences* 108:18960–18965.

9. Atkins, P., and J. de Paula, 2010. Atkins' Physical Chemistry. OUP Oxford.

10. Loughlin, R., R. Heald, and F. Nédélec, 2010. A computational model predicts Xenopus meiotic spindle organization. *The Journal of Cell Biology* 191:1239–1249.

11. Nédélec, F., and D. Foethke, 2007. Collective Langevin dynamics of flexible cytoskeletal fibers. *New Journal of Physics* 9:427.